PAPER

Surface-enhanced Raman imaging of cell membrane by a highly homogeneous and isotropic silver nanostructure†

Gianluigi Zito,* Giulia Rusciano, Giuseppe Pesce, Alden Dochshanov and Antonio Sasso

Label-free chemical imaging of live cell membranes can shed light on the molecular basis of cell membrane functionalities and their alterations under membrane-related diseases. In principle, this can be done by surface-enhanced Raman scattering (SERS) in confocal microscopy, but requires engineering plasmonic architectures with a spatially invariant SERS enhancement factor $G(x, y) = G$. To this end, we exploit a self-assembled isotropic nanostructure with characteristics of homogeneity typical of the so-called near-hyperuniform disorder. The resulting highly dense, homogeneous and isotropic random pattern consists of clusters of silver nanoparticles with limited size dispersion. This nanostructure brings together several advantages: very large hot spot density ($\sim 10^4$ μm^{-2}), superior spatial reproducibility (SD < 1% over 2500 μm^2) and single-molecule sensitivity ($G_{av} \sim 10^9$), all on a centimeter scale transparent active area. We are able to reconstruct the label-free SERS-based chemical map of live cell membranes with confocal resolution. In particular, SERS imaging is here demonstrated on red blood cells *in vitro* in order to use the Raman-resonant heme of the cell as a contrast medium to prove spectroscopic detection of membrane molecules. Numerical simulations also clarify the SERS characteristics of the substrate in terms of electromagnetic enhancement and distance sensitivity range consistently with the experiments. The large SERS-active area is intended for multi-cellular imaging on the same substrate, which is important for spectroscopic comparative analysis of complex organisms like cells. This opens new routes for *in situ* quantitative surface analysis and dynamic probing of living cells exposed to membrane-targeting drugs.

Introduction

Confocal micro-Raman spectroscopy[1,2] allows label-free chemical recognition of molecular species by identifying their average vibrational fingerprint in diffraction-limited volumes. In addition, the advantage of correlative scanning microscopy allows 'Raman imaging' of biological species. However, low scattering efficiency of biological samples limits the potential of this technique. Beyond spontaneous Raman, surface-enhanced Raman scattering (SERS) enables huge Raman enhancements reaching single-molecule sensitivity.[3,4] The Raman gain relies on resonant plasmon excitations in noble metal nanostructures which amplify the local electromagnetic

field.[5] The electromagnetic SERS enhancement factor G depends on the active substrate's architecture,[6–12] but detection efficiency is also affected by the excitation/collection process, environment/surrounding conditions,[8] molecular affinity to the metal,[13] molecular photostability,[14] and stochastic spatial distribution[15] of the molecules adsorbed in proximity to the so-called hot spots.[16,17] Despite the complexity of SERS phenomenology, SERS has found successful application in cutting-edge bio-chemical and medical research.[18,19] As for instance, the SERS technique has proved to be an effective platform for optical probing and imaging of live-cells *via* SERS nanotags[20–23] or in label-free experiments for surface cell sensing,[24,25] typically with colloidal substrates of nanoparticles (NPs) which are capable of high SERS sensitivity and density of hot-spots not achievable by lithographic nanostructures. However, two important difficulties arise in colloidal-based schemes that may cloud the interpretation of the experimental label-free signal when aiming at SERS imaging of the cell surface: (i) the plasmon-amplified signal from the surface emitters is mixed with the unavoidable unamplified Raman signal emitted from the molecules in the surrounding volume.

Department of Physics, University of Naples Federico II, via Cintia, 80126-I Naples, Italy. E-mail: zito@fisica.unina.it; Fax: (+39) 081 676352; Tel: (+39) 081 676273

The spatially average SERS enhancement factor G_{av} is typically several orders of magnitude lower than the hot-spot maxima[8,15] G_{max}, therefore, in general, the simultaneous contribution in the scattering volume from spontaneous conventional Raman (CR) photons is not negligible and must be quantitatively assessed on a case-by-case basis during SERS experiments. Thereby, the actual signature of plasma membrane biomolecules can be difficult to isolate against inner cell molecules *via* SERS spectroscopy of living cells. As clearly pointed out by several SERS studies of red blood cells (RBCs),[27–29] SERS detection of erythrocyte membrane is far more difficult because the Raman-resonant hemoglobin (Hb)[30,31] present in the RBC volume may totally mask the membrane signal. (ii) Furthermore, typical colloidal SERS substrates suffer from insufficient spatial reproducibility due to their local geometric heterogeneity which induces an uncontrollable position-dependent enhancement $G(x, y)$.

Although great efforts have been dedicated in the last few decades to the synthesis and fabrication of high performance SERS substrates in terms of sensitivity and reproducibility,[6–12,18,19,25,26] little attention has been paid to devise transparent SERS substrates capable of a 'spatially flat' enhancement factor $(G(x, y) = G)$ on a large-area and simultaneously capable of accurate surface imaging at the single cell scale (confocal detection). Recently, Yamazoe *et al.*[25] demonstrated large-area SERS imaging of brain tissue by using a low-cost, random gold nanostructure. However, since their approach relied on using a large laser spot size (6 μm), of course, they did not deal with SERS imaging at the single cell scale that requires confocal resolution, nor did they discuss the role of isotropy induced by the nanostructure's disorder.[32] Furthermore, for challenging bio-systems like RBCs, very large SERS sensitivity is required to detect membrane glycoproteins and glycolipids.[28] While RBC membrane contributions have been identified under particular conditions,[28,29] glycolipid/protein-sensitive SERS imaging of live RBC membrane has not been reported yet, except for a previous study in which we reported part of our preliminary results.[33]

Herein, we achieve a very uniform plasmonic amplification thanks to a random close-packed pattern of silver NP-clusters (nanoislands) characterized by a spatial homogeneity and isotropy close to the so-called hyperuniform disorder.[34–39] We take advantage of hyperuniformity metrics,[34] useful for studying the actual degree of order in periodic and glass systems, for a quantitative characterization of our random nanoisland's pattern. Such a pattern is based on the self-assembling of metal-loaded block copolymer (BCP) micelles in a highly concentrated solution. Overall, our method brings in several advantages: very large hot-spot density ($\sim 10^4$ μm^{-2}), superior spatial reproducibility (SD < 1% over 2500 μm^2) and single-molecule sensitivity, all on a centimeter scale transparent active area. The random close packing is a consequence of the nanoislands' density increasing. Surprisingly, instead of reducing SERS spatial reproducibility, it favors a higher uniformity of the SERS enhancement factor and a higher amplification. The single molecule sensitivity of our substrates is demon-

strated by using the two-analyte SERS method.[40] Moreover, the direct comparison between CR and SERS analyses of RBC ghosts in twin experiments indicates an enhancement factor of up to $G_{av} \sim 10^9$. We apply our SERS substrates for live-RBC sensing aiming to ascertain both the potential of SERS imaging and effective sensitivity to the challenging RBC membrane. In fact, we prove the membrane molecules to be detected against Hb in the surrounding volume by axially scanning the live-cell and by using Hb as a Raman contrast medium. Remarkably, SERS spectra are characterized by glycoprotein and glycolipid contributions not masked by membrane-bound Hb. We also carry out Finite Element Method (FEM) numerical simulations to clarify the SERS substrate characteristics in terms of electromagnetic enhancement and distance sensitivity range. The results are consistent with the experimental negligible cytosolic Hb contribution to the SERS spectra. Finally, we show, for the first time, the SERS-based, label-free chemical imaging of live RBC membrane *in vitro*. Given the molecular complexity of a cell, a robust SERS correlative imaging will be advantageous for eliciting membrane chemical information by differential analysis between control cells and cells expressing specific biomarkers or exposed to external stimuli and drug treatments.

Results and discussion

Synthesis and characterization of the nanoclusters' random close-packing

Fractal aggregates are among the most efficient scattering enhancers because the formation of clusters with favorable geometries induces strong cascade amplification into gap hot-spots.[41,42] Central to high SERS performance is also the maximization of the spatial density of hot spots. We have selected the engineering characteristics of our SERS substrate to combine both. To this end, block copolymer-based self-assembling of clusters of nanoparticles is ideal. We started from the fabrication of the hexagonal periodic template of silver NP clusters proposed by Cho *et al.*[12] It is based on the immediate long-range self-assembling of block-copolymer (BCP) micelles of polystyrene-*block*-poly-4-vinylpyridine (PS-*b*-P4VP) loaded with silver nanoparticles (Ag-NPs). The self-assembling is directed by fast solvent evaporation *via* spin-coating. Cho *et al.*[12] applied this method using a silicon crystal wafer as the supporting material. However, a preferential choice for membrane sensing is inverted Raman microscopy in back-scattering configuration, for which silicon is not applicable. Thus we moved to a transparent supporting material.

We first reproduced on glass the same protocol of ref. 12 in which the packing periodicity of the BCP micelles was imposed by varying the relative chain lengths of the block copolymers of PS and P4VP, respectively defining the micelle's shell and core. We used 24 mm × 24 mm commercial coverslips as shown in Fig. 1A. A typical TEM image of the resulting Ag-BCP film obtained on glass with PS-*b*-P4VP of molecular weight 10 400-*b*-19 200 is shown in Fig. 1B. Each nano-island
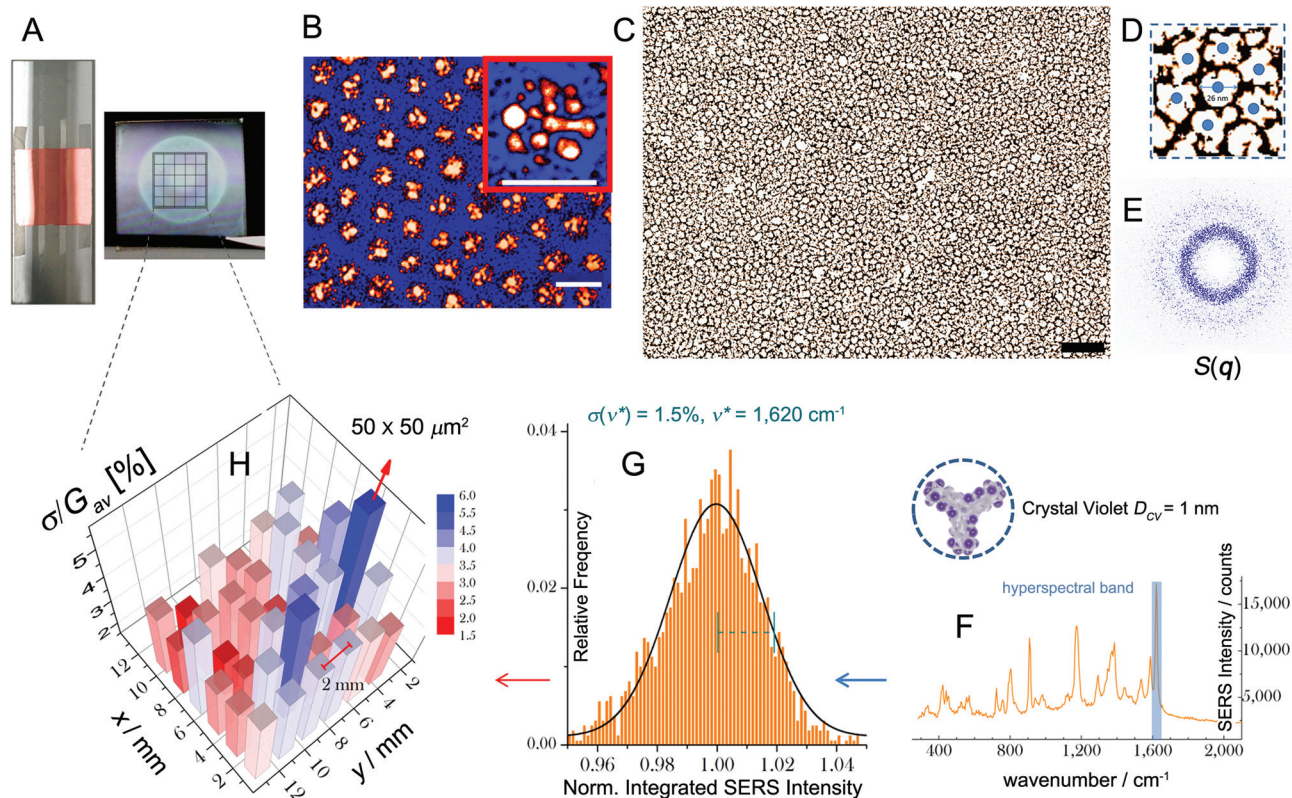
Fig. 1 Characterization of the SERS substrate. (A) Photographs of the large-area transparent SERS substrate on glass (24×24 mm^2). (B) TEM micrograph of the lower density hexagonal nanostructure (false color) used as the initial morphology of the SERS substrate pattern. The inset shows, in detail, a cluster of Ag-NPs. (C) TEM micrograph of the final random pattern obtained by applying our protocol: the filling fraction is highly increased inducing nanoisland gaps of 2–3 nm, as shown in the close-up (D). (E) Characteristic ring-shaped structure factor $S(q)$ of the random nanostructure (C): it shows radial isotropy and high homogeneity, the latter evidenced by $S(q \to 0) \simeq 0$. (F) Typically observed SERS spectrum of the CV molecule used to build the map $G(x, y)$. (G) Example of narrow normal distribution of SERS intensities measured by sampling an area of 2500 µm^2. (F) Map of the relative standard deviation SD $= \sigma/G_{av}$ of the enhancement factor $G(x, y)$ by spatial sampling the CV spectrum in a regular grid of 1 cm^2: the SERS enhancement factor is spatially flat everywhere. Scale bars are 50 nm in (B), 26 nm in the inset of (B) and 150 nm in (C).

consisted of nearly touching (or in contact) nanoparticles of size d in the range ~1–12 nm (Fig. 1B and inset) with equivalent size dispersion on a large scale. The average nanoisland diameter was $D \sim 26$ nm, while cluster height was $h \sim 14$ nm. However, as a consequence of the different de-wetting properties of the polymer on borosilicate glass used as the supporting substrate, in our case the hexagonal pattern was characterized by a gap $g \sim 15$–20 nm between the NP-islands, against the ~8 nm gap found on silicon wafer in ref. 12. This effect reduced the spatial density of clusters. Thus we modified the protocol achieving better performances on glass by adopting a different approach to impose higher density packing. This was done not by changing the chemical composition of the block-copolymer micelles, but acting on the polymer concentration and spin coating speed, always with micelles of PS-b-P4VP of molecular weight 10 400-b-19 200. Our variant of Cho's method increased the nano-islands' packing density by processing a higher concentrated Ag-BCP solution with centrifugation, filtration and slow spin coating treatment as described in the Methods section. Our procedure removed the limitation imposed by the PS-shell thickness, probably

because of PS unfolding on glass in agreement with previous studies of Krishnamoorthy et al.[43] Therefore, the formation of PS sheets embedding the Ag-P4VP produced a monolayer of immobilized Ag nano-domains ($D \sim 26$ nm, $h \sim 14$ nm) with the gap down to $g \sim 2$ nm, as shown in Fig. 1C and D. After UV exposure, our on-glass plasmonic substrates revealed an optical coating quality with a reflective green glow at ambient light (Fig. 1A, right panel). The increased cluster density produced a distortion of the hexagonal lattice. However, the resulting random nanoisland pattern (Fig. 1C) gave superior SERS performances, up to one order of magnitude in terms of both spatial reproducibility and enhancement factor despite the lack of periodicity (as discussed in the next section). Therefore, we decided to study the morphological characteristics of the random pattern following the work of Torquato et al. about hyperuniform disorder.[34–39]

In brief, a two-dimensional point pattern is hyperuniform in terms of order metrics if the local number fluctuation $\sigma^2(R)$ of the point pattern, measured in a circular window of radius R, grows according to $\sim R$ instead of the pattern area $\sim R^2$ on a large length scale.[34,35] This property points out a hidden order

in the pattern, which can also be studied, in the reciprocal space, by the small-q behavior of the structure factor $S(q)$. An ideal hyperuniform pattern must be characterized by zero infinite-wavelength density fluctuations of the point pattern, *i.e.*, $S(q \rightarrow 0) = 0$ or, in other words, vanishing fluctuations on a large length scale that can be used to quantify the degree of homogeneity.[36] Ideal periodic structures are trivially hyperuniform but cannot be spatially isotropic.[34] On the other hand, disordered patterns, which are isotropic, can also be hyperuniform under particular conditions. In other words, they can be extremely homogeneous despite the random nature of their pattern and an example is the so-called maximally random jammed packing of hard spheres.[37] We therefore studied the structure factor map $S(q)$ of our random nanostructure, calculated through discrete Fourier transform (for $q \neq 0$) following ref. 38 as described in the ESI.† The structure factor map is depicted in Fig. 1E and appears to be characterized by a double ring shape with $S(q \rightarrow 0) \simeq 0$. The overall map features are in agreement with those reported by Florescu *et al.* about hyperuniform disordered photonic crystal patterns.[39] The radial profile of the structure factor with its distinctive feature of linearly suppressed infinite-wavelength density fluctuation[37,38] is shown in Fig. S1 in the ESI.† From the linear fit of the radial average $S = a_0 + a_1 Q$, with normalized spatial frequency $Q = qD/2\pi$, we find an extrapolated value $S(0) = a_0 = 0.0006 \pm 0.0004$, with linear coefficient $a_1 = 0.110 \pm 0.003$. When compared to ref. 38, these values strongly suggest the onset of a condition close to hyperuniform disorder in the nanoislands' pattern. This structural information allows one to quantify the amount of homogeneity achieved in the random structure.[36] In our case, it says that our random nanoisland's structure is as spatially homogeneous as a periodic one.

Spatially flat enhancement factor

The large-area characterization of the SERS intensity response over the random nanostructure (Fig. 1C) demonstrated a spatially flat substrate enhancement factor[9] G_{av}. We measured the SERS spectrum produced by the analyte molecule of tris(4-(dimethylamino)phenyl)methylium chloride (crystal violet, CV) of which an example is shown in Fig. 1F. The excitation wavelength was chosen at $\lambda_o = 532$ nm (Fig. S2†). We deposited a monolayer of the testing molecule (CV) with quantifiable concentration per unit area taking care of obtaining a high uniformity on a large scale. To this end, we developed a reproducible methodology based on slow water evaporation (this aspect is described in the Methods section and a scheme is also depicted in Fig. S2†). In order to avoid bias in the SERS enhancement factor evaluation, particular care was required for measuring an accurate CR intensity as a normalization value. Indeed, we verified that incorrect CR normalization based on CV powder used for CR measurements[12] leads to a highly overestimated enhancement $G_{av} \sim 10^8$–10^9. An appropriate normalization was carried out on diluted CV water solution to take into account the strong absorption of the solid CV having a penetration length of only ≈ 30 nm at $\lambda_o = 532$ nm.

Moreover, underestimation of the Raman reference caused by CV photobleaching in CR (it can be of a factor ~ 20, Fig. S3†) was avoided by adopting an incident power and integration time of the same order of SERS measurements (see ESI† for a detailed analysis). This CV characterization finally led to a substrate average enhancement factor given by $G_{av} = 1.04 \times 10^6 \pm 3.6\%$. The error of 3.6% is obtained from the relative std. dev. SD $= \sigma/G_{av}$ after sampling the SERS signal on a very large area. In particular, the sampling of CV SERS spectra was repeated *via* raster scans in 36 regions evenly spaced by 2 mm, for a total of $\simeq 90\,000$ positions covering 1 cm². Each region had an area of 50×50 μm² and was sampled typically with 1 μm spacing. For uniformity characterization, the substrate was probed by depositing a number of molecules per cluster estimated to be $N_m \simeq 145$ (see the Methods section), for a total of $\simeq 96\,000$ molecules in each laser spot which defined the scattering area $A_{scat} = 0.44$ μm². The SERS intensities were normally distributed, as shown in Fig. 1G. Relative standard deviations SD $= \sigma/G_{av}$ over local areas were in the range 0.9%–5.6% as shown in Fig. 1H, with a mean value of 3.6%. This local spatial fluctuation of the SERS signal is remarkably below any reported data. The full area (1 cm²) relative standard deviation was then <30% despite the colossal scale of characterization.

Prior to the application of our protocol, the BCP template solution originally gave the regular hexagonal pattern shown in Fig. 1B, for which a similar characterization pointed out one order of magnitude reduced spatial reproducibility as limited to 9%–20% over analogous local regions of 50×50 μm², besides a ~ 6-fold lower average enhancement factor due to the lower packing density, as preliminarily reported in ref. 33. In both samples (hexagonal and random), the unitary nanoislands have near equivalent geometric characteristics as they result from the same process of nucleation in the BCP micelles which limits the NP size dispersion. This fact alone favors a reproducible SERS response in both structures and is improved by the averaging process over many clusters in the scattering area (0.44 μm²), namely ~ 240 in the hexagonal pattern against ~ 520 in the random pattern. The larger density of clusters in the latter is estimated to account for a reduction of the SERS fluctuation SD at most of 47% by roughly evaluating the square root ratio between the number of nanoislands present in the scattering area. Therefore, in order to explain the improvement of a factor ~ 5–10 (from 9%–20% to 0.9%–5.6% in the spatial reproducibility), a higher homogenization of the electromagnetic field in the denser random pattern is likely to play a significant role for suppressing point-to-point SERS fluctuations. In fact, in the hexagonal lattice, given the relative large gap (15–20 nm) between the clusters against the small size of the NPs (1–12 nm), the inter-cluster coupling due to near field interaction is not very strong, in agreement with ref. 9 and also confirmed by our simulations (see the Numerical simulations of the enhancement factor). Therefore, for the hexagonal pattern, the gap region only marginally contributes to the SERS enhancement and structural imperfections can alter more importantly the average electromagnetic enhancement in

a given scattering area. Instead, in the random close packed structure ($g \sim 2$–3 nm), the near field interaction is significantly larger and homogeneously distributed everywhere. In addition, isotropy introduced by disorder is likely to promote the uniformity of SERS response. Overall, the high spatial homogeneity and isotropy allow averaging more effectively the electromagnetic response excited in the laser beam waist, eventually suppressing the point-to-point SERS fluctuation.

Single-molecule sensitivity by two-analyte technique

We explored the SERS substrate's sensitivity limit by applying the two-analyte statistics approach.[40] The single-molecule sensitivity was validated by uniformly depositing a diluted solution of combined CV and Rhodamine 6G (R6G) in order to have a total of $\simeq$300 molecules in each scattering area, in a molar ratio 5 : 1 to take into account their different differential Raman cross sections[44] at the excitation wavelength of 532 nm – in fact, the frequency of detection of the two molecules resulted balanced at this ratio. We acquired the SERS response in 20 000 positions over an area of $\sim$1 cm^2 and analyzed the related statistics of coincidence produced by the peaks centered at 1650 cm^{-1} (range 1638–1670 cm^{-1}) and 1620 cm^{-1} (range 1605–1630 cm^{-1}), distinctive features, respectively, of R6G and CV. The null-detection data were filtered out retaining 4832 spectra. The statistics was then obtained by projecting *via* Basis Analysis the spectra ensemble along the two pure-molecule spectra chosen as basis functions (see the Methods section). The low probability of mixed events indicated clearly the single-molecule regime as evident from Fig. 2.

Numerical simulations of the enhancement factor

We studied the induced electromagnetic enhancement by means of 3D numerical FEM-based simulations of the full electrodynamic problem in local approximation. Mainly constrained by computational limits, our study was confined to

single or coupled clusters in a dimer configuration with a gap of 3 nm (Fig. 3A) approximating the experimental nano-aggregates observed *via* TEM (Fig. 1B and C) (see the Methods section). We believe that this simplified model can capture the essential features in terms of distance sensitivity range since we find only a minor contribution to the average enhancement factor due to inter-cluster coupling (Fig. S4†). Given the random nature of the clusters, we studied 30 configurations observed by TEM and AFM. The representative results reported here are based, in particular, on the cluster geometry obtained from TEM (see Fig. 1B (inset)) and AFM measurements[33] (see the Methods section). The basic characteristics of the various clusters in terms of electromagnetic enhancement and distance sensitivity range were found common to all.

In brief, we find that the electromagnetic localization collectively gives rise to broadband plasmon response thanks to the large intra-cluster coupling[45] and plasmon hybridization[46] (Fig. 3B). The spatially averaged enhancement G_{av} obtained from our simulations is even larger than 10^9 on a wide range of excitation wavelengths (Fig. 3C). Local maxima G_{max} are up to $\sim$10^{12} in chain configurations of strongly interacting NPs, in agreement with predictions of cascade amplification.[41] The inter-cluster coupling among close clusters is found to increase the volume fraction of near-field above a certain threshold as shown in Fig. S4,† but this effect has minor consequence on the value of the enhancement factor spatially averaged in the immediate vicinity of the clusters (see the Methods section). This is in agreement with the recent report by Yan *et al.*,[9] in which ordered arrays of NP clusters were studied as a function of their distance and where only a limited increase (by a factor $\simeq$2–3) of G_{av} was found under strong inter-cluster coupling.

Finally, we explored the dependence of the perceived enhancement on the distance between the metal and the molecules by defining a hindrance shell. This represents a proximity limit to the nanosurfaces around the cluster's center. By calculating the spatially averaged enhancement factor as a function of its radius R_S, we can determine approximately the decay of the perceived enhancement with the distance. The mean enhancement G_{av} is found to decrease by 4 orders of magnitude around a critical radius, $\sim$2 nm above R_S = 12 nm, namely just on the outer surface of the cluster ($h \simeq$ 14 nm), indicating that the field is highly localized in the inner dielectric volume, which we term a high-G shell (Fig. 3D). This dramatic distance dependence might also affect the measured substrate enhancement depending on the probability of the molecules to penetrate the high-G shell. From the normalized integral of the distance curve $G_{av}(R_S)$ depicted in Fig. 3D, we calculated an effective length of interaction limited to only $\sim$4 nm above the high-G shell. We conclude that the characteristic length scale of the electromagnetic enhancement decay is mainly governed by the length scale of the cluster subunits, *i.e.*, the single nanoparticles. By repeating the experimental enhancement factor estimation with CV molecules deposited on the SERS substrate with an intact polymer, namely $\sim$5 nm above the cluster surface, the experimental
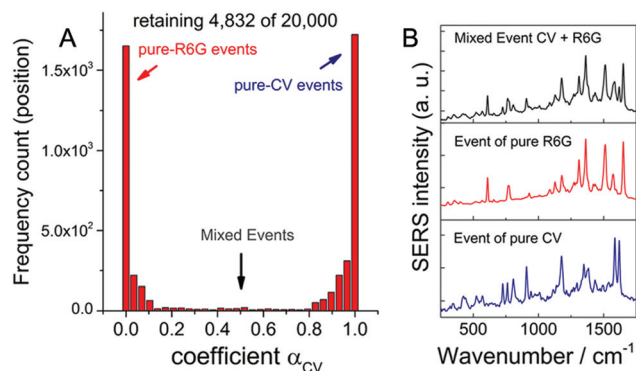
Fig. 2 Single-molecule sensitivity by two-analyte SERS characterization. The low detection probability of mixed-CV-R6G events experimentally demonstrates the single-molecule sensitivity of our SERS substrate. The graph in (A) shows the frequency count of the non-null detected SERS spectra (acquired by scanning the substrate over 1 cm^2) as a function of the basis coefficient along the pure-CV spectrum. (B) Examples of pure-dye spectra and mixed two-dye spectrum.
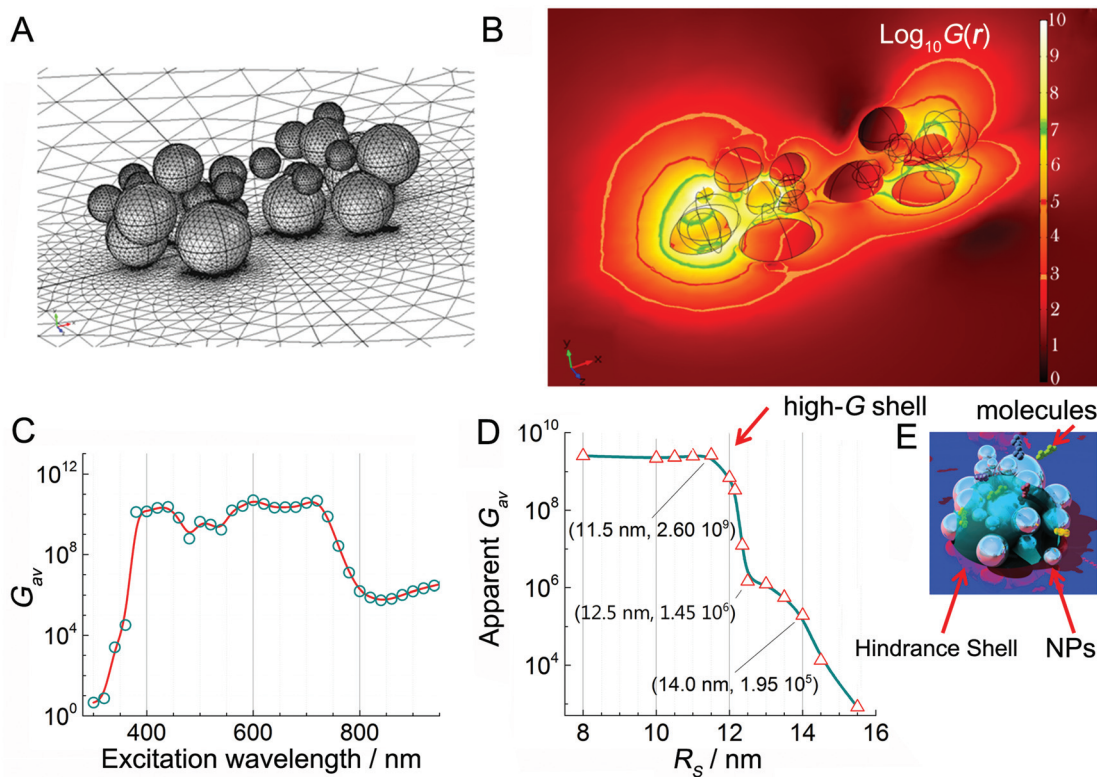
Fig. 3 Modeling of electromagnetic SERS enhancement factor by FEM. The essential characteristics of the electromagnetic enhancement are studied by modeling several clusters of Ag-NPs approximating the geometries experimentally observed via TEM (see Fig. 1B–D). (A) Representative 3D model of a dimer of clusters. (B) Approximated enhancement factor map $G = |E_s/E_i|^4$ in the cut planes x–y and x–z (log-scale), as produced by (A), upon averaging on all incident polarizations, for excitation wavelength $\lambda_o = 540$ nm (i.e., an intermediate value between the excitation and Raman wavelengths): the colored counter lines mark the field amplification progressively decreasing far from the hot-spots. (C) The spatially averaged enhancement factor G_{av} is larger than 10^9 thanks to the strong NP coupling: the clustering seems to provide the benefit of broadband responsiveness due to plasmon resonance hybridization. (D) Apparent G_{av} as a function of the hindrance shell radius R_S to simulate the dramatic dependence of SERS gain on the distance between molecules and inner hot-spots of the clusters (at 540 nm): the length scale decay is governed by the small nanoparticle size. (E) A cartoon of the hindrance shell around a cluster of NPs.

SERS enhancement appeared reduced by approximately 3 orders of magnitude, in agreement with the simulation.

Enhancement factor estimation with RBC ghost

In view of a study on RBC membranes, we carried out preliminary measurements on a solution of RBC ghosts[47] prepared from cellular extracts in PBS solvent (10 mg ml^{-1}) following ref. 29. We employed such a RBC ghost solution for a differential analysis of Hb-free cells and live cells for the Raman assignment and cross-check identification of the membrane's spectral features detected during SERS experiments on the viable RBC. Nonetheless, we found it very useful to evaluate the SERS enhancement factor G_{av} also on RBC ghosts since it was more similar to the viable RBCs of our interest. In twin experiments with SERS coated glass and a simple coverslip used in a sandwiched cell infiltrated with identical RBC ghost solution, we experimentally observed a SERS line intensity, at the lipid marker frequency 1436 cm^{-1} (characteristic of the membrane), as large as $\simeq$2000 photon-counts with an incident power $P_{in} = 3$ μW and integration time $\Delta t = 200$ ms, against a

CR spectral line intensity of 200 photon-counts (at same Raman frequency) measured at $P_{in} = 33$ mW and $\Delta t = 10$ s. The ratio between these signals was further normalized to the ratio between the estimated number of emitters in the two measurements (SERS against CR). This was done by considering an effective height of the SERS scattering volume of $\approx$10 nm, against a CR confocal depth of 2.6 μm (see the Methods section). Thus we estimated in the SERS region a fraction equal to $10/2600 = 0.4\%$ of the molecules in the CR scattering volume, leading to $G_{av} \simeq 1.4 \times 10^9$. This analytical enhancement factor is significantly larger than the enhancement factor estimated with CV ($G_{av} \sim 10^6$). However, the dramatic distance dependence of the SERS enhancement factor (Fig. 3D) might provide a simple explanation of why CV and RBC ghosts gave rise to these different SERS efficiencies. Molecules are brought randomly to probe the distribution of the enhanced electromagnetic field. Thus, the response of the substrate can be importantly affected by the molecular affinity or environmental conditions of the analyte (type of solvent, pH, ionic strength, molecular aggregation)[8,13] which can change

the mean distance of interaction, hence the probability of finding molecules closer to the hot spots. It is worth noting, in fact, that the average enhancement estimated with RBC ghosts ($G_{av} \sim 10^9$) is in agreement with the theoretical G_{av} achievable for molecules close enough to the high-G shell (Fig. 3D). In addition, the different measured enhancement factors might also depend on the different intrinsic emitting properties of CV and RBC membrane molecules in proximity to the NPs.[48,49] The strong absorption band of CV at the excitation wavelength[50,51] at 532 nm does not allow an accurate estimation of the absolute value of G_{av}, but, of course, allows an accurate estimation of the SERS spatial reproducibility, provided that the acquisition is fast enough to avoid photobleaching during the scansion. On the other hand, the nanostructure's efficiency of amplifying RBC membrane scattering can be more accurately quantified by the analytical SERS enhancement factor evaluated on RBC ghosts.

Axial scanning of RBC to validate membrane detection

Plasma membrane in RBCs is fundamental for the functionality of the cell.[52] As for instance, membrane deformability changes in relation to blood diseases[53,54] and its functional glycoproteins determine the cell interaction with the bioenvironment.[55,56] Therefore, SERS detection of RBC membrane would be advantageous, although challenging because of Hb presence.[27] Actually, we took advantage of the Hb protein content in the inner volume of the cell and its particular Raman sensitivity at λ_o = 532 nm for demonstrating the large SERS sensitivity of our substrate and membrane molecule detection. We identified unambiguously that the SERS signal was produced by the plasma membrane molecules on the Ag-nanostructure using the cytosolic Hb, clearly identifiable *via*

Raman, as a contrast medium. RBCs directly extracted by healthy donors prior to the experiments were infiltrated in two sealed sandwiched coverslip cells, one made of uncoated coverslips and the other with a SERS coated coverslip on one side. RBCs were left to adhere by physisorption to the simple coverslip for CR measurements (to the SERS coated coverslip for SERS measurements) in an isotonic solution for 30 min with no further treatment. We did not observe hemolytic activity of our immobilized SERS nanostructure on the time scale of the measurements, as described in the ESI.† SERS data acquisition in back-scattering configuration with inverted microscope excitation was possible by taking advantage of the transparency of the SERS substrate. We previously measured the effective thickness of the confocal scattering volume obtaining the value h_{eff} = 2.6 μm (see the Methods section and ESI†). In twin separate experiments, one with RBC on the SERS substrate and the other with RBC on a simple coverslip, we repeatedly acquired Raman spectra at different heights by scanning along the z-axial coordinate, as represented in Fig. 4A and B. By means of this characterization, we ascertained that the experimental Raman intensity acquired with the SERS substrate was actually localized only at the cell surface by correlating the maximum intensity position with the active nanocoating position ($z = 0$). Indeed, we observed a peaked behavior of the SERS intensity (Fig. 4B, red points) spatially located around the nanostructure height with an effective depth of ~800 nm, *i.e.*, well below h_{eff}. We acquired SERS spectra with incident power so low that, when penetrating the cell volume, the Raman signature of cytosolic Hb was not even identifiable on the background noise. The excitation power was P_{in} = 3 μW and integration time Δt = 100 ms. Thus, we excluded the possibility that any contribution from the cytosolic heme could be mixed to the SERS signal.
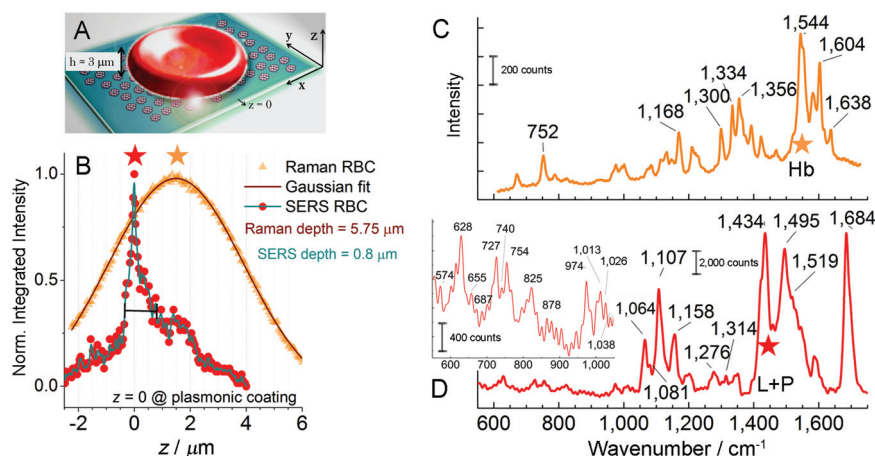

Fig. 4 Axial Raman scanning of RBC to validate membrane detection. (A) Schematic representation of the experiment: Raman excitation and collection (from the RBC) is obtained *via* inverted confocal microscopy in backscattering geometry. (B) The SERS intensity integrated over 1400–1600 cm^{-1}, from the RBC, is localized sharply along the axial coordinate z around the SERS nanostructure position ($z = 0$) (red points); in contrast, the CR signal gives rise to a broad signal in z – peaked at the RBC equatorial plane located ~1.5 μm above the glass (yellow points) – as a result of the volumetric scattering contribution. (C) CR spectrum of RBC, which shows typical spectral features of Hb[29–31] (corresponding to yellow star curve in (B)). (D) Typical SERS spectrum measured at $z = 0$, which clearly presents spectral markers of membrane lipids (L) and proteins (P) (corresponding to red star curve in (B));[55–59] inset in (D) shows a magnified view of the smaller spectral features.

Overall, excitation power and integration time had to be increased by 3 orders of magnitude prior to inducing any 'bulk'-contribution in CR measurements. In fact, the analogous axial response curve measured on RBC on the uncoated coverslip (CR) required at least P_{in} = 500 μW and Δt = 1 s, and was characterized by a significant broader bell shape given by the intrinsic convolution of the signal with the cell volume (Fig. 4B, yellow points), peaked around the middle plane of the cell (z = 1.5 μm). As expected, this Raman spectrum was mainly ascribable only to hemoglobin, as characterized by the typical spectral features of the heme group,[30,31] and was found unvaried at the z-coordinate around the membrane (example shown in Fig. 4C). In contrast to CR detection, surface SERS spectra (z = 0) had a clearly different Raman fingerprint characterized by membrane peaks not observed in previous SERS studies of RBCs[27–29] (Fig. 4D and 5).

Raman assignment

Since membrane thickness is limited to ~5 nm, membrane-bound Hb present in the interaction range of the active Ag-NPs could mask other non-Raman-resonant membrane constituents at 532 nm excitation. Brazhe *et al.* found that membrane-bound Hb dominated SERS signals.[27] On the other hand, other studies have identified in the less resonant excitation at 785 nm and in the higher SERS enhancement factor of their SERS substrate, the favorable conditions at which SERS amplification may exalt membrane contributions (proteins and lipids) not masked by membrane-bound Hb.[28,29]

In our experiments, the CR spectrum of the live RBC reflected only volume Hb, regardless of the particular excitation spot within the cell (Fig. 4C, see also a detailed spectrum in Fig. S5† and related assignment table in the ESI†).
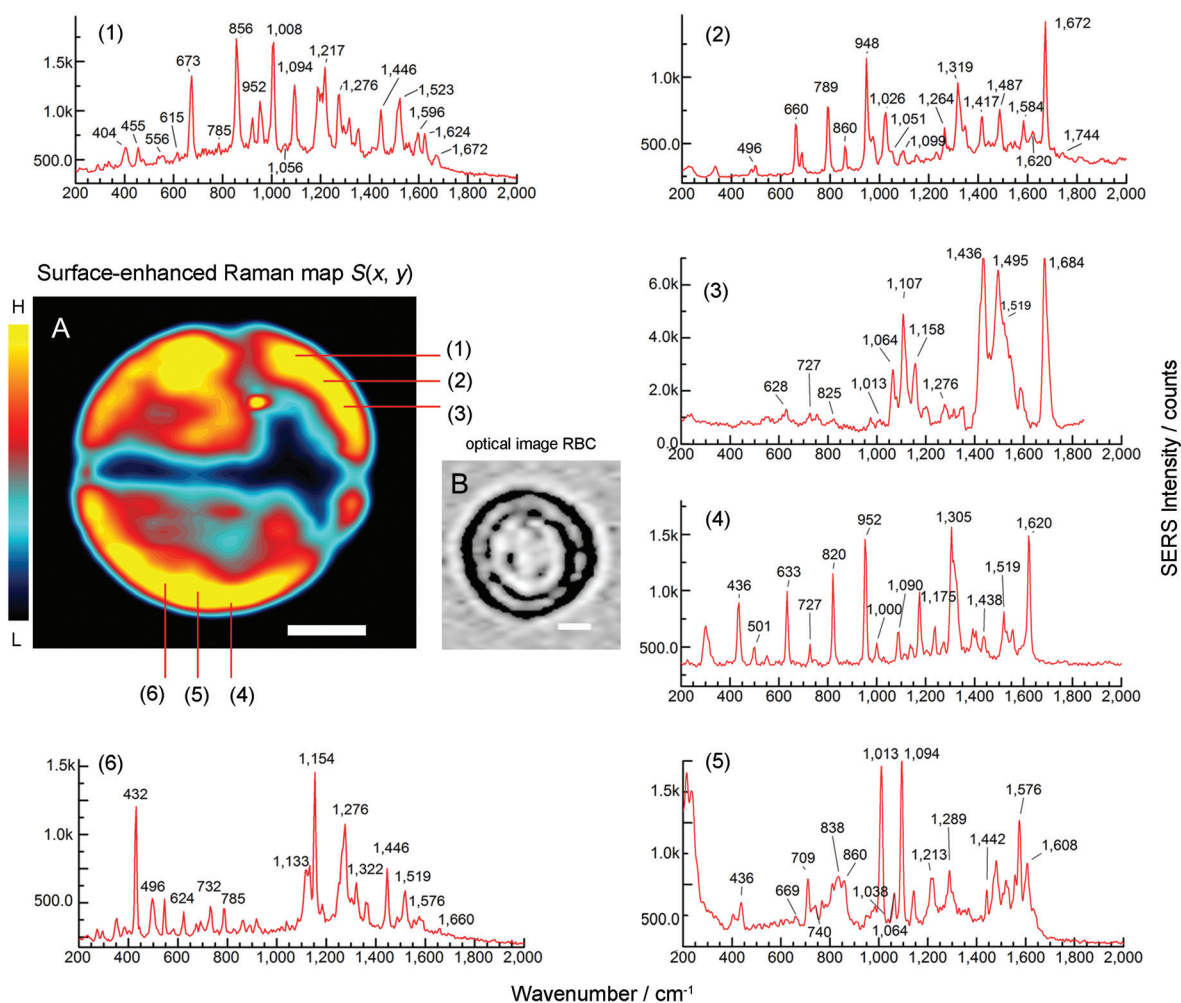
Fig. 5 Reproducible correlative scanning of erythrocyte membrane *via* SERS. (A) Hyperspectral SERS map $S(x, y, z = 0)$ resulting from scanning the particular cell shown in (B) (optical image); the map is obtained by integrating the SERS intensity over a wide range of frequencies (1100–1700 cm^{-1}) to account for all principal spectral features (Δt = 2 s per pixel over an area of 2500 pixels). The map reproduces the morphology of the cell with astonishing fidelity, thus demonstrating the quality of the SERS correlative scanning achieved through our SERS substrate thanks to its spatially flat enhancement factor (Fig. 1C). Representative SERS spectra from RBC membrane acquired in different positions (1)–(6) according to the labels: 'surface' spectral features are remarkably different from the 'volume' Raman spectrum shown in Fig. 4C. Scale bar = 4 μm in (A) and (B).

Instead, the SERS spectra $S(x, y, z = 0)$ acquired on the viable RBC showed spectral features remarkably different from the CR spectrum of the cell (e.g., see Fig. 4D and 5). The SERS spectra $S(x, y, z = 0)$ were characterized by extremely sharp peaks with a large signal/noise ratio having line intensities and spectral markers comparable with those observed on the RBC ghost solution under equivalent conditions. In addition, they showed spectral features clearly dependent on the particular position of the laser spot on the cell, and in a reproducible fashion. Given the enormous experimental enhancement of the SERS substrate and its theoretical short interaction range (~4 nm), we expected to detect via SERS the live-RBC membrane phospholipids, proteins and glycocalyx features.[55–59] Therefore, for an accurate Raman assignment, we decided to compare our live-RBC SERS spectra with those acquired on an erythrocyte ghost solution measured both under SERS and CR conditions.

By CR analysis of erythrocyte ghosts, we did not observe significant contributions produced by membrane-bound Hb. In contrast, we observed clear markers of lipids, amino acids and carbohydrates (Fig. S6†), in agreement with previous reports.[47,57] Hence, we did not expect to observe enhanced Hb features in SERS experiments on RBC ghosts (in contrast with ref. 27). In fact, we found a good agreement between the SERS spectrum of the RBC ghost (Hb-free), the latter shown in Fig. S7,† with CR spectral lines of the RBC ghosts (Fig. S6†), with no typical markers of membrane-bound Hb (the tables accompanying each spectrum reported in the ESI† summarize the main spectroscopic assignment with further details). Thus, we expected to detect membrane features, not masked by Hb, also in SERS experiments on the live-cell. A representative SERS spectrum on viable RBC is shown in Fig. 4D. Limiting our research to membrane-specific spectral markers, we focused primarily on the phospholipid/carbohydrate component which was unambiguously identified and appeared in the major part of the spectra, clearly evidenced by the skeletal modes at 1062, 1085, 1126 cm^{-1} and CH$_2$ twist and bend modes at 1296 and 1436 cm^{-1}.[60,61] In addition, carotenoid spectral components (embedded in the cellular membrane)[57,62] were clearly evident in the SERS spectra at 1156 and 1515–1527 cm^{-1}, as can be seen in Fig. 4D. By inspecting Fig. S7,† SERS spectra acquired on viable cells and ghosts show overlapping spectral lines. Such features also match the CR spectrum of RBC ghosts (Fig. S6†). In addition, Fig. S7–S9 in the ESI† clearly show a complex variety of protein, lipid and carbohydrate features acquired in different positions of the viable cell, and point out a sensitivity to the local membrane environment, as further discussed later.

The bottom line is that lipid, carbohydrate and amino acid SERS spectral features found on the live RBC, which demonstrate membrane sensitivity even at 532 nm, are likely the result of the very large average SERS enhancement factor $G_{av} \sim 10^9$ and limited SERS interaction length (~4 nm). However, given the stochastic process of membrane interaction with the substrate, of course, occasional membrane-bound Hb contributions in the SERS spectra of the viable cell cannot be totally excluded, and can be regarded as membrane features as well. It is worth mentioning that the possible ghost formation or Hb release was monitored during SERS measurements by repeatedly inspecting the sample by optical microscopy. Membrane ruptures were evident and produced Hb microaggregates near RBC ghosts only after exposure to non-immobilized, citrate-reduced silver colloids used in control experiments. In contrast, we did not observe ghost formation with our immobilized nanostructure (ESI†). The absence of hemolytic activity for short-term exposure (up to 2 h) was supported by the spectroscopic observation of mainly Hb-free SERS signals. On the other hand, oxidative stress of the membrane due to nanosilver is very likely to occur and can be actually inferred from the relative peak intensities of lipid markers in the range 1060–1110 cm^{-1} of Fig. S7(a) in the ESI.† However, this pattern was not systematically evident in the SERS spectra.

CR- and SERS-based chemical imaging of live RBC

Finally, we acquired SERS (or CR) spectra by spatially scanning the cell surface (or volume) for hyperspectral imaging and correlation with simultaneous optical microscopy. In SERS experiments, the incident power P_{in} was always kept below 50 μW whereas the integration time per pixel (Δt per pxl) of the grid was varied in the range 0.02 s–10 s, depending on the scan. Typical incident power P_{in} was in the range 0.5–12 μW for SERS imaging. No visible damage was observed under these conditions.[31] In the case of very fast acquisition (integration time as low as 20–100 ms), we observed temporal fluctuations in the SERS spectral intensities with characteristic peak-wanderings (in particular for membrane spectral features at 1013, 1436, 1656, 1668 cm^{-1}). SERS intensity fluctuations were, instead, totally absent in the test measurement with the CV analyte. Hence, we interpreted them as the result of two main mechanisms: (i) the modulation of the distance between the SERS nanostructure and the cell membrane due to the local membrane fluctuation like undulation;[53,63] (ii) possible membrane molecular diffusion[63] such as protein dynamic exchange and re-assembling.[64] In particular, about the first dynamics, it is worth noting that the adhesion distance between the plasma membrane and the supporting glass substrate is expected to be in the range of 3 nm.[65] Therefore, combined with an enhancement of the signal strongly dependent on the average distance from the clusters (Fig. 3D), such a dynamic is actually expected to provide a source of variability in the experimental SERS signal. Therefore, due to the observed temporal variation, for hyperspectral SERS imaging the SERS spectra $S(x, y, z = 0)$ were time-averaged with a long-enough integration time of ~2–10 s at each scan position (x, y). In such a way, the spectral characteristics measured at each point were found to be reproducible. A confocal, lateral spatial resolution of ~200 nm was experimentally determined (see the Methods section). As aforementioned, the SERS spectra $S(x, y, z = 0)$ showed spectral features with a large signal/noise ratio that we assigned mainly to carbohydrates, proteins and phospholipids of the membrane (see the Raman assignment section). As depicted through the representative SERS spectra

(1)–(6) of Fig. 5, each membrane position was characterized by a different SERS spectrum, denoting a sensing capability for the local molecular environment explored in the laser scattering area. It must be pointed out that such a circumstance, typical in other kinds of cells, is not trivial in the case of RBCs given the typical dominant contribution of Hb distributed everywhere in the cell, and points out a spatially-resolved SERS detection of RBC plasma membrane. In contrast, CR scan spectra revealed only the typical Raman signature of deoxy-Hb in each position. Nonetheless, in that case, the intensity of the Raman signal, depending on the number of molecules intersected in the scattering volume, followed the volumetric morphology of the cell characterized by hemoglobin molecules preferentially distributed along the cell periphery (Fig. S5†).

The representative hyperspectral map shown in Fig. 5A is calculated by integrating the SERS intensity in a wide range of wavenumbers, *i.e.*, 1100–1700 cm^{-1}, to account for the major spectral features, and reveals a strong correlation with the optical image of the RBC actually scanned (Fig. 5B). Remarkably, we found the SERS continuum background[66,67] to be continuously, and reproducibly, modulated in correlation with the cell surface morphology. Such background broad scattering contributed to exalting the morphology of the membrane reproduced by the hyperspectral representation in Fig. 5A. We believe this contribution of SERS background modulation to be produced by the enhanced fluorescence of the inner-cell molecules modulated by the distance from the nanostructure imposed by the RBC biconcave morphology. This aspect will be discussed elsewhere. The SERS imaging was finally possible because of the excellent uniformity of the enhancement factor of the nanostructure.

substrate on erythrocyte cells which represent a simplified cellular model constituted by a plasma membrane vesicle full of hemoglobin, a Raman-resonant molecule that we used as contrast to demonstrate the membrane sensitivity. The phospholipid bilayer fingerprint and glycoproteins' spectral features are in fact identified in the SERS spectra because of the high average enhancement factor ($\simeq 10^9$) of the nanostructure, experimentally measured on a solution of RBC ghosts and consistent with the electromagnetic enhancement predicted by FEM numerical simulations. In perspective, label-free chemical imaging with time-resolution potential could unveil fundamental mechanisms for the cell membrane. Differential analysis between control and diseased cells might allow monitoring the dynamics of the cell surface molecular regulation under external mechanical stimuli or drug exposure with the benefit of visualizing possible effects. Given the complexity of SERS spectra in biological systems, SERS reproducibility is fundamental and the imaging capability added to multivariate statistical techniques[68,69] might shed light on membrane molecular processes. In this direction, we are currently expanding the study on red blood cells to discriminate the molecular variation induced at the membrane during the life cycle of the cell and under mechanical stress induced into a microfluidic channel. Generally speaking, plasma membrane interactions play a key role in molecularly targeted therapy. Therefore, we are also working on the SERS imaging of specific induced protein expression into cancer cells, which can be helpful for early diagnosis. In this direction, loading gold NPs into BCP micelles with the same protocol used for silver is expected to produce highly performing SERS substrates with larger biocompatibility.

Conclusion

In summary, we have demonstrated a successful approach for membrane label-free SERS imaging on living red blood cells *in vitro* based on a random close-packed pattern of silver nanoclusters used as SERS substrates: a first but crucial step towards quantitative SERS imaging analysis of the complex chemistry of a bio-membrane. Like displaying an optical image on a digital screen with uniform illumination allows capturing its essence, displaying the chemical information of the cell membrane by a uniform plasmonic enhancement allows implementing more sophisticated analyses based on simultaneous correlative scansion imaging. Such a uniform 'illumination' is here demonstrated with a large density of clusters of nanoparticles arranged in a highly homogeneous and isotropic pattern. This favors the suppression of the point-to-point SERS variance producing a large-area SERS enhancement factor with unprecedented spatial reproducibility, even working at confocal resolution (beam waist $\approx$370 nm). A low-cost, transparent SERS-active nanocoating with high reproducible sensitivity over a centimeter scale enables practical experiments and allows acquiring sound statistic information on many cells on the same SERS substrate. We apply our SERS

Methods

Ag-BCP synthesis and deposition

BCP of PS-*b*-P4VP with molecular weights of 10 400-*b*-19 200 and polydispersity index 1.27 was purchased from Polymer Source Inc. All reagents are from Sigma Aldrich. A solution of tetrahydrofuran (THF) (7.0 g) and toluene (10.5 g) (*i.e.*, ratio 0.67 w/w), for a total volume of 20 ml, was used for the micelle formation of PS-*b*-P4VP (97.2 mg) in a relative concentration of 0.55% w/w under stirring at 700 rpm for 3 h at 25 °C, then for 2 h at 67 °C, before slowly cooling down the solution at room temperature. The micelles were loaded *via* a coordination complex of the P4VP core with Ag$^+$ starting from 203.7 mg of AgNO$_3$, in molar ratio 2 : 1 with the former, upon stirring (700 rpm) for 24 h. We filtered the excess of material with 200 nm PTFE syringe filters before the reduction procedure with NaBH$_4$. The amount of NaBH$_4$ dramatically affected the quality of the suspension. The Ag$^+$-P4VP was best reduced predissolving 440 mg of fine dry powder of NaBH$_4$ in the same solvent THF/toluene (4.4 ml) under a controlled atmosphere with low humidity. Only 440 μl of such a solution was then added dropwise to the Ag$^+$-P4VP solution, followed by stirring (24 h). Very important was the filtering of the black solution

finally reached with 200 nm PTFE syringe filters to restore a solution, black wine-coloured, and large aggregate-free. This solution was centrifuged at 11 krpm for 20 min to separate the possible unloaded supernatant micelles. In a 1 ml eppendorf, the supernatant removed was 300 μl. This left a more concentrated solution of nanocomposite micelles, ~0.77% w/w. The remaining solution was sonicated for 22 min. A volume of 100 μl was left over the supporting glass for 30 s before starting the spin-coating at 1.0 krpm speed for 60 s, under a controlled ambient atmosphere. This allowed us to achieve an extremely uniform film coating with nanoisland gaps $g < 5$ nm. UV exposure at 254 nm (Hg lamp, Sankyo Denki G15T8) at a sample distance of 6 cm, for ~20 h and with an energy density of 1.7 mJ cm^{-2}, removed the copolymer. The achieved reddish plasmonic film on glass appeared as a transparent optical coating with a green backscattering glow (Fig. 1A). The film homogeneity and adhesion to the glass was unaffected when soaking it into solutions of water, methanol, ethanol and acetone. Extinction spectra were repeatedly acquired to check the correspondence between UV/Vis measurements (Perkin Elmer UV-Vis-spectrometer Lambda 35, equipped with integrating sphere) and SERS performances as an indicator test before and after polymer removal: the extinction spectra were, respectively, characterized by broad curves peaked around 430–440 nm and 470–500 nm with tails up to 650 nm. After UV treatment, and subtracting the supporting coverslip contribution, the absorption coefficient peaked at 485 nm, while the scattering coefficient peaked at 515 nm with a long tail towards the IR region.

Morphological characterization

Neat micelle solutions were characterized by Dynamic Light Scattering (DLS) and Small Angle X-ray Scattering (SAXS). A narrow diameter distribution around an average value of $D_{micelle} = 37.2 \pm 0.5$ nm (DLS) with a spherical parameter 0.73 (for ideal sphere is 0.75) (SAXS) was found. Atomic force microscopy (AFM) characterization (in tapping mode) of the film revealed a highly regular lattice denoting an average height of the nanofeatures of $h \sim 13.6$ nm, presumably corresponding to bumps' morphology over a bottom PS-layer.[43] For TEM, both films of pristine PS-b-P4VP and Ag-BCP nanocomposite were backed with a carbon film, floated off on water with poly(acrylic acid) backing and mounted on copper grids. TEM micrographs were analyzed by custom-made Matlab Mathworks codes based on Voronoi–Delaunay triangulation. Each silver cluster contained, on average, 12–20 NPs with diameters of 1–12 nm, with a collective equivalent diameter $D = 26 \pm 2$ nm, confined by the P4VP cores of the same size approximately. The gap g was found reduced down to 1–5 nm by decreasing the spin-coating speed and increasing the micelles' concentration. Given an expected contribution to the gap due to the PS-shell thickness according to $g = D_{micelle} - D \sim 2 \times 5.5$ nm = 11 nm, an experimental gap as low as $g \sim$ 2–3 nm between the metal nanoislands (~P4VP cores) pointed out the PS-corona unfolding on the glass surface. This is in agreement with what is reported for film assembling of PS-b-

P2VP micelles on glass, forming a continuous residual layer on the surface due to partial fusion of the coronal PS-blocks of adjacent micelles.[43] The height estimated via AFM (13.6 ± 2.0 nm) was comparable to ~D/2. Therefore, 2–3 piled layers of nanoparticles (NPs) were likely to be arranged in a hemispherical bunch shape, i.e., the model used for simulations.

Hyperspectral confocal Raman microscopy

Raman/SERS spectra were acquired with a micro-Raman system WiTec Alpha 300, endowed with a spectrometer equipped with two diffraction gratings with 600 and 1800 g mm^{-1} providing a resolution, respectively, of 3.6 and 1.5 cm^{-1}. Backscattering light collection and detection were recorded, respectively, through a Nikon 60× dry objective (NA = 0.8 and WD = 300 μm) and a deep-depletion, back-illuminated Andor CCD camera (DV401A-BV-352) (1024 × 400 pixels) operating at −60 °C. The confocal conditions were imposed by the core (acting as a pin-hole) (25 μm) of the multimode fiber delivering the signal to the spectrometer. The probed scattering area on the sample A_{scat}, constrained by confocal detection in the backscattering collection, was accurately measured independently to be $\pi w_o^2 = 0.44$ μm^2 (beam waist $w_o = 373 \pm 3$ nm) with a knife-edge technique (see the next section). A three-axis piezo-nanopositioner allowed precise control of the sampling translation with nanometer accuracy over a maximum range of 100×100 μm^2. For larger areas, a coarse translation was added by using the mechanical micrometer of the microscope stage. Positioning, area mapping and acquisition were controlled via computer. All experiments were conducted with an inverted microscope configuration.

Preliminary dye deposition and SERS characterization

Crystal violet was diluted into a Milli-Q water solution to several concentrations, namely 0.3, 3.1, 34.6, 43.8, 150, 380, 4200, 54 000 nM. Then, the particular solution employed was infiltrated into a cell constituted by two parallel substrates (24×24 mm^2) distanced by spacers and sealed. The procedure left a homogeneous layer of molecules adsorbed on the Ag-NPs. Details can be found in the ESI, Fig. S2.† A volume of 100 μl of a 380 nM solution of CV, distributed over an area of 24×24 mm^2 = 576 mm^2, produced a number of molecules $N_{surf} = 8683$ (halved value because of two adsorbing surfaces) within the scattering area of 0.44 μm^2. Given the effective diameter[70] $D_{CV} \simeq 1$ nm of the CV molecule covering an approximate area of 0.785 nm^2, and the number of molecules N_{surf} estimated in the scattering area, the molecular filling fraction of the probed area was only ~1.5% (less than one monolayer). Given $D = 26$ nm and average $g = 3$ nm, it corresponded to a number of molecules per cluster $N_m = 17$. For the spatial reproducibility test, a concentration of 4.2 μM was deposited with the same approach producing a number of molecules in 0.44 μm^2 of $\simeq$95 990, corresponding to a number of molecules per cluster $N_m = 185$. The enhancement factor of the substrates was estimated under the conditions of molecular deposition described above, namely $N_{surf} = 8683$. Raman enhancements were evaluated by using the definition of the SERS substrate

enhancement factor[8] according to $G = \dfrac{I_S/N_{surf}}{I_R/N_{vol}}$, where I_S and I_R are the SERS and CR amplitudes of one Raman peak, respectively. N_{surf} and N_{vol} are the number of molecules estimated in the scattering area and volume, respectively contributing to the signals I_S and I_R. In particular, we estimated G by considering the ratio I_S/I_R of the CV bands at 914, 1175 and 1620 cm^{-1}. Both scattering area and scattering volume were measured by a knife-edge-like technique on a silicon wafer with sharp edge by using the same Raman intensity of the 520 cm^{-1} silicon band. Three-dimensional nano-positioning thanks to a piezo-scanner (in-plane resolution of 3 nm and 0.2 nm axial) allowed us to determine the scattering volume, giving A_{scat} = 0.44 μm^2, h_{eff} = 2.6 ± 0.2 μm (following Cai et al.[71]), and finally $V_{scat} \approx 2.0$ μm^3 after integration of the Gaussian beam volume. Hence, for evaluating G, the Raman reference signal I_R of CV was normalized to the number N_{vol} following the procedure described in the ESI,† due to the strong absorption of CV molecules at 532 nm (having a molar extinction coefficient[51] approximately of 0.5 × 10^5 cm^{-1} M^{-1}) and CV photostability issues. The experimental values were: I_S = 256 counts, with an incident power P_{in} = 3.7 μW and integration time Δt = 1 s, from N_{surf} = 8683. The reference was: I_R = 216 counts, with 69 μW of power for 10 s and from N_{vol} = 4.07 × 10^7. Therefore, we estimated a value G_{av} = 1.04 × 10^6 ± 3.6% (SD is given as the mean value over the 36 raster scan areas). For the two-analyte SERS statistics, a water solution diluted at 12 nM of CV and R6G in a molar ratio 5 : 1 was deposited as described above starting from a total volume of 100 μl over 2 × 576 mm^2. The characterization with dyes was conducted on the final dry samples. Null detection spectra were filtered out by using a custom code (MATLAB, The MathWorks Inc.) based on the variance of the spectra. Only data with Raman intensities producing an overall variance >5-fold the variance of the noise signal (previously determined) were processed for the statistics of coincidence. The incident power was set at 50 μW and Δt = 100 ms.

Enhancement factor from RBC ghost solution

In this case, we estimated the effective number of molecules in the SERS scattering (effective) volume as those in a volume $A_{scat} \times h_{SERS}$ where h_{SERS} is an effective SERS height given by the sum of the effective length of interaction (∼4 nm) above the high-G shell (Fig. 3D) plus a fraction of the cluster height (conservatively 40%) that the molecules can fill, thus giving h_{SERS} = 4 nm + 0.4 × 14 nm ≈ 10 nm. The ratio of the confocal effective Raman height and SERS height h_{eff}/h_{SERS} gives an approximation of the molecular number ratio expected between the two measurements.

SERS hyperspectral imaging

The erythrocytes were collected from the blood stream and injected into a phosphate buffer saline solution (∼300 mOsm L^{-1}) in a ratio of 50 : 1000 v/v, then infiltrated into a sealed planar cell of thickness 20 μm formed by a top coverslip and a bottom SERS substrate. After 30–60 min, the erythrocytes floating in Brownian motion were found in contact with the bottom plasmonic surface. Experiments had a typical duration <2 h. SERS chemical maps were acquired on several erythrocytes per substrate, with a power incident on the sample in the range 0.1–42 μW, that is at a laser intensity comprised between a value as low as 23 W cm^{-2} and a maximum of 1 × 10^4 W cm^{-2}. The integration time Δt was varied, depending on the experiment, from 0.02 s up to 10.0 s for time-averaged spatial signals.

Finite element method simulations

The typical cluster configuration resulting from the micelle nucleation of the Ag-NPs was designed by reproducing the TEM observation. Two-layer aggregates of 12 NPs with diameters from 5 to 12 nm (approximating the experimental observation) in a hemispherical bunch shape placed on the supporting glass were taken into account. Both water and air were used as environments. Fig. 3 shows calculations in water. We used Johnson and Christy's silver dielectric functions.[72] Extra-fine FEM-based mesh was computed with Comsol Multiphysics 4.3a, avoiding lighting rod effects with a resolution of curvature of 0.3 nm, a maximum growth rate of 1.35, a minimum element size of 0.9 nm and the resolution of narrow region 0.85. A second mesh was included for the smaller regions with a minimum element size of 0.1 nm. The FEM simulations were carried out as a function of the incident wavelength, from λ = 300 nm to 1000 nm ($\delta\lambda$ = 20 nm), and as a function of the polarization of the incident field of amplitude E_i. Given the random orientation of the dipoles (dimers) of NPs within the cluster, the total scattered field of amplitude $E_s(r)$ was averaged over the incident polarization orientation (10 orientations, plane waves linearly polarized in the substrate plane). The minimum separation between nanoparticles was set to 0.5 nm or coalescent nanoparticles were designed in order to avoid an unrealistic enhanced field and the need for a non-local or quantum theory.[73] The maximum value of the field enhancement achievable in close NPs resulted in $|E_{s,max}/E_i|$ = 1500 for a minimum gap of 0.5 nm (hot-spot maximum enhancement ∼10^{12}). The spatial distribution of the electromagnetic field was found unvaried, as for the absolute intensity of the field, after having slightly changed the mesh-size, or upon repeated calculations. The inner spherical domain of simulation had a radius of 300 nm with 10 outer shells of perfectly matched layers (PML) and outer scattering boundary conditions. No field reflection at the boundary was found. The spatially averaged enhancement factor and the dependence on the average distance from the clusters (Fig. 3C and D, respectively) were calculated by averaging over a regular hexagonal prism of volume V_u of side 16.2 nm and height 25.0 nm around the cluster ($h \simeq 14$ nm), i.e., a confining box on the glass substrate to which the NP volume was subtracted. Given the short range topological order with a hexagonal centred symmetry (Fig. 1D), the box V_u could be seen as the modelling unitary cell. Independent clusters gave rise to very similar simulated behaviours. Also dimers of equivalent clus-

ters were considered (having a minimum gap $g = 3$ nm). In that case the volume was set at $2V_u$. Additional information about inter-cluster coupling effect is provided in the ESI.†

Acknowledgements

Notes and references

1 K. Kong, *et al.*, *Proc. Natl. Acad. Sci. U. S. A.*, 2013, **110**, 15189.
2 M. Okada, *et al.*, *Proc. Natl. Acad. Sci. U. S. A.*, 2012, **109**, 28–32.
3 K. Kneipp, *et al.*, *Phys. Rev. Lett.*, 1997, **78**, 1667–1670.
4 E. C. Le Ru and P. G. Etchegoin, *Annu. Rev. Phys. Chem.*, 2012, **63**, 65–87.
5 S. J. Lee, Z. Guan, H. Xu and M. Moskovits, *J. Phys. Chem. C*, 2007, **111**, 17985–17988.
6 X. Lin, Y. Cui, Y. Xu, R. Bin and Z. Tian, *Anal. Bioanal. Chem.*, 2009, **394**, 1729–1745.
7 G. A. Baker and D. S. Moore, *Anal. Bioanal. Chem.*, 2005, **382**, 1751–1770.
8 E. C. Le Ru and P. G. Etchegoin, *Principles of Surface-Enhanced Raman Spectroscopy and Related Plasmonic Effects*, Elsevier, Amsterdam, The Netherlands, 2009.
9 B. Yan, *et al.*, *ACS Nano*, 2009, **3**, 1190–1202.
10 N. A. Hatab, *et al.*, *Nano Lett.*, 2010, **10**, 4952–4955.
11 D. Lim, *et al.*, *Nat. Nanotechnol.*, 2011, **6**, 452–460.
12 W. J. Cho, Y. Kim and J. K. Kim, *ACS Nano*, 2012, **6**, 249–255.
13 P. Pinkhasova, L. Yang, Y. Zhang, S. Sukhishvili and H. Du, *Langmuir*, 2012, **28**, 2529–2535.
14 P. G. Etchegoin, P. D. Lacharmoise and E. C. Le Ru, *Anal. Chem.*, 2009, **81**, 682–688.
15 E. C. Le Ru, P. G. Etchegoin and M. Meyer, *J. Chem. Phys.*, 2006, **125**, 204701.
16 A. M. Michaels, J. Jiang and L. Brus, *J. Phys. Chem. B*, 2000, **104**, 11965–11971.
17 P. Alonso-González, *et al.*, *Nat. Commun.*, 2012, **3**, 684.
18 S. Schlücker, *Angew. Chem., Int. Ed.*, 2014, **53**, 4756–4795.
19 W. Xie and S. Schlücker, *Rep. Prog. Phys.*, 2014, **77**, 116502.
20 C. L. Zavaleta, *et al.*, *Proc. Natl. Acad. Sci. U. S. A.*, 2009, **106**, 13511–13516.
21 X. Qian, *et al.*, *Nat. Biotechnol.*, 2007, **26**, 83–90.
22 J. Kneipp, H. Kneipp, A. Rajadurai, R. W. Redmond and K. Kneipp, *J. Raman Spectrosc.*, 2009, **40**, 1–5.
23 M. D. Hodges, *et al.*, *ACS Nano*, 2011, **5**, 9535–9541.
24 B. Yan and B. M. Reinhard, *J. Phys. Chem. Lett.*, 2010, **1**, 1595–1598.
25 S. Yamazoe, M. Naya, M. Shiota, T. Morikawa, A. Kubo, *et al.*, *ACS Nano*, 2014, **8**, 5622–5632.
26 N. G. Greeneltch, M. G. Blaber, A.-I. Henry, G. C. Schatz and R. P. Van Duyne, *Anal. Chem.*, 2013, **85**, 2297–2303.
27 N. A. Brazhe, *et al.*, *Biophys. J.*, 2009, **97**, 3206–3214.
28 W. R. Premasiri, J. C. Lee and L. D. Ziegler, *J. Phys. Chem. B*, 2012, **116**, 9376–9386.
29 D. Drescher, T. Buechner, D. McNaughton and J. Kneipp, *Phys. Chem. Chem. Phys.*, 2013, **15**, 5364–5373.
30 K. M. Marzec, *et al.*, *ChemPhysChem*, 2014, **15**, 3963–3968.
31 B. R. Wood and D. McNaughton, *J. Raman Spectrosc.*, 2002, **33**, 517–523.
32 C. De Rosa, *et al.*, *Phys. Chem. Chem. Phys.*, 2015, **17**, 8061–8069.
33 G. Zito, *et al.*, *Proc. SPIE Optics+Optoelectronics*, 2013, **87740B**, 1.
34 S. Torquato and F. Stillinger, *Phys. Rev. E: Stat. Phys., Plasmas, Fluids, Relat. Interdisc. Top.*, 2003, **68**, 041113.
35 C. E. Zachary and S. Torquato, *J. Stat. Mech.: Theory Exp.*, 2009, **12**, P12015.
36 R. Xie, *et al.*, *Proc. Natl. Acad. Sci. U. S. A.*, 2013, **110**, 13250–13254.
37 C. E. Zachary, Y. Jiao and S. Torquato, *Phys. Rev. Lett.*, 2011, **106**, 178001.
38 Y. Jiao, *et al.*, *Phys. Rev. E: Stat. Phys., Plasmas, Fluids, Relat. Interdisc. Top.*, 2014, **89**, 022721.
39 M. Florescu, S. Torquato and P. J. Steinhardt, *Proc. Natl. Acad. Sci. U. S. A.*, 2009, **106**, 20658–20663.
40 P. G. Etchegoin, M. Meyer, E. Blackie and E. C. Le Ru, *Anal. Chem.*, 2007, **79**, 8411–8415.
41 K. Li, M. I. Stockman and D. J. Bergman, *Phys. Rev. Lett.*, 2003, **91**, 227402.
42 A. Gopinath, *et al.*, *Nano Lett.*, 2009, **9**, 3922–3929.
43 S. Krishnamoorthy, R. Pugin, J. Brugger, H. Heinzelmann and C. Hinderling, *Adv. Funct. Mater.*, 2006, **16**, 1469–1475.
44 S. A. Meyer, E. C. Le Ru and P. G. Etchegoin, *J. Phys. Chem. A*, 2010, **114**, 5515–5519.
45 R. Esteban, R. W. Taylor, J. J. Baumberg and J. Aizpurua, *Langmuir*, 2012, **28**, 8881–8890.
46 H. Wang, D. W. Brandl, P. Nordlander and N. J. Halas, *Acc. Chem. Res.*, 2007, **40**, 53–62.
47 R. B. Mikkelsen, S. P. Verma and D. F. Wallach, *Proc. Natl. Acad. Sci. U. S. A.*, 1978, **75**, 5478–5482.
48 A. M. Kern, A. J. Meixner and O. J. Martin, *ACS Nano*, 2012, **6**, 9828–9836.
49 D. A. Weitz, S. Garoff, J. I. Gersten and A. Nitzan, *J. Chem. Phys.*, 1983, **78**, 5324–5338.
50 J. Korppi-Tommola and R. W. Yip, *Can. J. Chem.*, 1981, **59**, 191–194.

51 W. H. J. Storkg, J. M. Lippitsa and M. Mandel, *J. Phys. Chem.*, 1972, **76**, 1772–1775.

52 N. Mohandas and P. G. Gallagher, *Blood*, 2008, **112**, 3939–3948.

53 Y. Park, *et al.*, *Proc. Natl. Acad. Sci. U. S. A.*, 2008, **105**, 13730–13735.

54 A. C. De Luca, *et al.*, *Opt. Express*, 2008, **16**, 7943–7957.

55 T. Steck, *J. Cell Biol.*, 1974, **62**, 1–19.

56 B. Alberts, *et al.*, *Molecular Biology of the Cell*, Garland Science, New York, 4th edn, 2002.

57 J. L. Lippert, L. E. Gorczyca and G. Meiklejohn, *Biochim. Biophys. Acta, Biomembr.*, 1975, **382**, 5157.

58 J. De Gelder, K. De Gussem, P. Vandenabeele and L. Moens, *J. Raman Spectrosc.*, 2007, **38**, 1133–1147.

59 Z. D. Schultz and I. W. Levin, *Annu. Rev. Anal. Chem.*, 2011, **4**, 343–366.

60 B. P. Gaber, P. Yager and W. L. Peticolas, *Biophys. J.*, 1978, **21**, 161–176.

61 M. F. Mrozek and M. J. Weaver, *Anal. Chem.*, 2002, **74**, 4069–4075.

62 G. Rusciano, G. Pesce, M. Salemme, L. Selvaggi, C. Vaccaro, A. Sasso and R. Carotenuto, *Methods*, 2010, **51**, 22736.

63 U. Neugebauer, *et al.*, *ChemPhysChem.*, 2006, **7**, 1428–1430.

64 Y. Park, *et al.*, *Proc. Natl. Acad. Sci. U. S. A.*, 2010, **107**, 1289–1294.

65 A. S. Curtis, *J. Cell Biol.*, 1964, **20**, 199–215.

66 T. Itoh, V. Biju, M. Ishikawa and Y. Kikkawa, *J. Chem. Phys.*, 2006, **124**, 134708.

67 E. C. Le Ru, *et al.*, *J. Phys. Chem. C*, 2007, **111**, 16076–16079.

68 G. Rusciano, *et al.*, *PLoS One*, 2013, **8**, e72127.

69 G. Rusciano, *et al.*, *ACS Nano*, 2014, **8**, 12300–12309.

70 H. R. Arias, *et al.*, *Biochem.*, 2003, **42**, 7358–7370.

71 W. Cai, *et al.*, *Surf. Sci.*, 1998, **406**, 9–22.

72 P. B. Johnson and R. W. Christy, *Phys. Rev. B: Condens. Matter*, 1972, **6**, 4370–4379.

73 N. F. Van Hulst, *Nat. Nanotechnol.*, 2012, **7**, 775–777.